Vibrational Surface Electron-Energy-Loss Spectroscopy Probes Confined Surface-Phonon Modes

Hugo Lourenço-Martins and Mathieu Kociak*

Laboratoire de Physique des Solides, CNRS, UMR8502, Bâtiment 510, Université de Paris-Sud, France

(Received 31 July 2017; revised manuscript received 6 October 2017; published 7 December 2017)

Recently, two reports [Krivanek *et al.* Nature (London) **514**, 209 (2014), Lagos *et al.* Nature (London) **543**, 529 (2017)] have demonstrated the amazing possibility to probe vibrational excitations from nanoparticles with a spatial resolution much smaller than the corresponding free-space phonon wavelength using electron-energy-loss spectroscopy (EELS). While Lagos *et al.* evidenced a strong spatial and spectral modulation of the EELS signal over a nanoparticle, Krivanek *et al.* did not. Here, we show that discrepancies among different EELS experiments as well as their relation to optical near- and far-field optical experiments [Dai *et al.* Science **343**, 1125 (2014)] can be understood by introducing the concept of confined bright and dark surface phonon modes, whose density of states is probed by EELS. Such a concise formalism is the vibrational counterpart of the broadly used formalism for localized surface plasmons [Ouyang and Isaacson Philos. Mag. B **60**, 481 (1989), García de Abajo and Aizpurua Phys. Rev. B **56**, 15873 (1997), García de Abajo and Kociak Phys. Rev. Lett. **100**, 106804 (2008), Boudarham and Kociak Phys. Rev. B **85**, 245447 (2012)]; it makes it straightforward to predict or interpret phenomena already known for localized surface plasmons such as environment-related energy shifts or the possibility of 3D mapping of the related surface charge densities [Collins *et al.* ACS Photonics **2**, 1628 (2015)].

DOI: 10.1103/PhysRevX.7.041059

Subject Areas: Condensed Matter Physics, Plasmonics

Electron-energy-loss spectroscopy experiments consist of sending a free-electron beam onto a sample of interest and retrieving information on its excitations through the analysis of the energy lost by the electron beam. It can essentially be performed without spatial resolution at low electron energy (HREELS) or with a sub-angstrom resolution in a scanning transmission electron microscope (STEM). In a pioneering work, Ibach [1] used HREELS to analyze the vibrational excitations of a ZnO surface. He could retrieve the measured value of the surface phonon energy ω_s within what was later called the local continuum dielectric model (LCDM) [2]. This simple and powerful model relies on the assumption that the local dielectric constant $\epsilon(\omega) = \epsilon(\omega, q = 0)$ [where ω is the energy and $\epsilon(\omega)$ is equal to its value at zero transferred momentum q] is sufficient to describe electromagnetic excitations in a finite system. In Ibach's simple geometry, ω_s was such that $\epsilon(\omega_s) = -1$. Kliewer and Fuchs demonstrated the amazing efficiency of the LCDM to describe more complicated geometries, such as slabs [3] and infinite cylinders [4]. Already in these simple systems, the electromagnetic coupling between surfaces induces surface phonon splitting in so-called Fuchs-Kliewer (FK) modes with different charge distribution symmetries [Fig. 1(a)]. Most materials dielectric constants can be described in the optical phononic range with a Drude-Lorentz model requiring the sole knowledge of the longitudinal and transverse optical phonon energies (ω_{LO} and ω_{TO}) and the value of the dielectric constant at large energy values (ϵ_∞) of the bulk material; see the Appendix. One sees in Fig. 1(a) that surface phonon (SPh) modes disperse as a function of the transferred wave vector from ω_{TO} or ω_{LO} and converge to ω_s at large transferred wave vector.

The Fuchs-Kliewer work has been extended with impressive success [2] to the description of surface plasmons (SP) in simple systems such as slabs and cylinders [4,6] [see Fig. 1(b)]. As already described in Ref. [4], a practical reason for this success is the close resemblance between the dielectric constants of systems encompassing either optical phonons or plasmons (see the Appendix). Given similar electromagnetic boundary conditions, it is no surprise that similar physics is involved; in particular, surface waves, either SP or SPh can be regarded as surface charge density waves. However, such a resemblance is valid in a long-wavelength limit—precisely that of the LCDM. Of course, beyond the LCDM, which will not be evoked hereafter, the microscopic origin of the surface charge density waves is rather different at the atomic scale between SPs (free-electron charges) and SPhs (ion vibrations).

Stimulated by the development of the research on plasmons in nanoparticles systems, several simulation schemes basically relying on the LCDM [boundary element

*mathieu.kociak@u-psud.fr

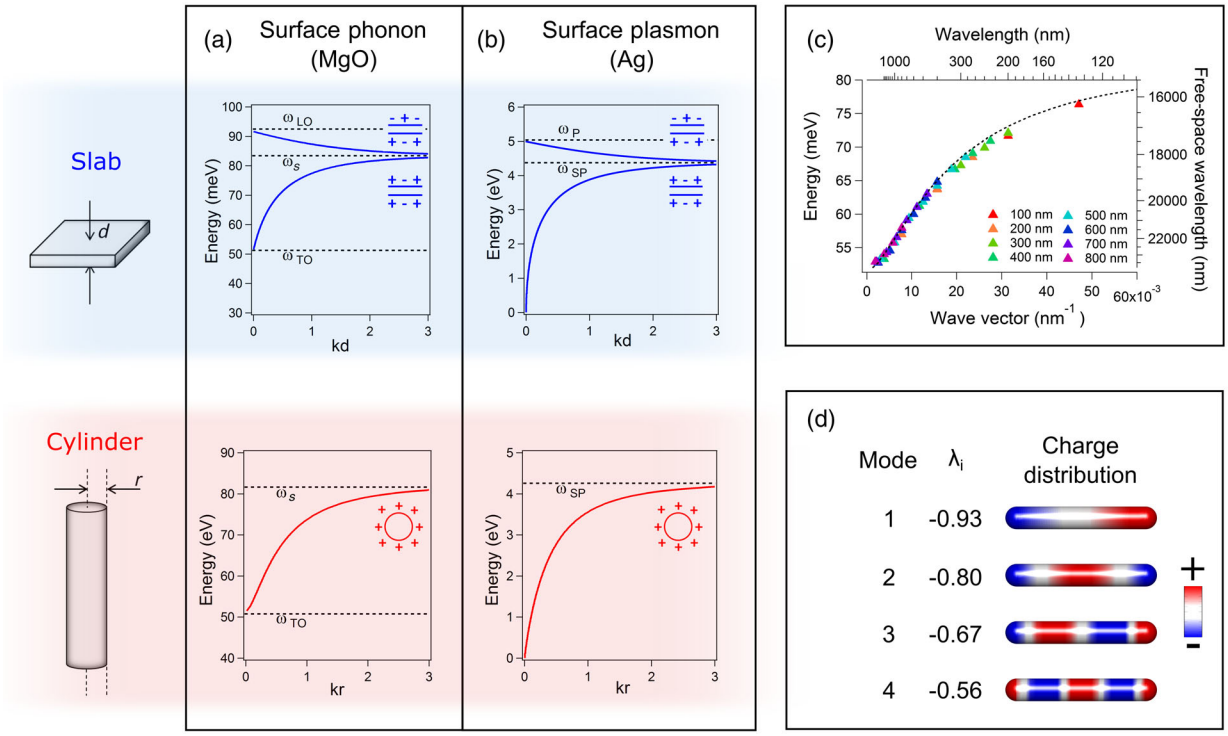

FIG. 1. Analogy between surface phonons modes and surface plasmons modes. (a) Dispersion relation of the Fuchs-Kliewer modes for a slab of thickness d (top) and a cylinder (bottom) of radius r made up of MgO. The charge symmetry of the modes is sketched in the inset. For the cylinder, only the rotationally invariant mode branch is shown, as the other modes are essentially not dispersing [5]. Calculations have been performed in the quasistatic approximation (b) Same for SP modes in silver. (c) Dispersion relation for the cSPh of nanorods, reconstructed from a series of retarded simulation of nanorods of different lengths (diameter is 30 nm). The dotted line is the quasistatic dispersion relation for an infinite cylinder of the same diameter, showing the remarkable agreement between both approximations even for long lengths of rods. (d) Surface eigencharge distribution for cSPh of a nanorod, with the given mode orders and eigenvalues λ_i.

method (BEM) [7–9] and discrete dipole approximation [10]] have been extensively used to simulate optical and EELS spectra dominated by localized SPs *confined* on nanoparticles. BEM simulations have been recently extended to the phonon range for STEM EELS [11] using the MNPBEM [12] implementation.

Now, beyond their unique simulation capabilities, LCDM-derived theories have offered a deep understanding of localized SP physics. In particular, they made explicit the link between STEM EELS and optical near-field spectroscopies as both are related to the electromagnetic local density of states (EMLDOS) [13,14] and showed that EELS is related to the extinction cross section for dipolar modes [15,16].

The goal of this paper is to show how the reasoning once made to explain SP confinement in nanoparticles and interpret STEM-EELS experiments can now be used to rationalize the interpretation of surface STEM-EELS vibrational experiments in nano-objects and predict new physical effects.

In the following, we introduce the confined surface phonons (cSPh) modes as surface phonons whose properties are mostly defined by the classical confinement that they experience in particles much smaller than the free-space equivalent wavelength. In this sense, if normal phonon modes are conceptually related to bulk plasmon modes and surface phonons to surface plasmons, cSPhs are the phononic counterpart to localized SPs. For the sake of simplicity, we neglect retardation in the following, unless otherwise specified. As we show, this is justified by the relatively small sizes of phononic nanoparticles studied in the literature [11,17]. A rigorous definition of the cSPh modes can then be given in the quasistatic (QS) approximation using a modal decomposition form, first introduced in the case of confined SPs [7,14,18]; see the Appendix. cSPhs are then defined as a set of eigencharges $\{\sigma_i\}$ and eigenvalues $\{\lambda_i\}$, i being the mode index. In the general case, λ_i, which depends only on the geometry of the nanoparticle, has to be determined numerically, and corresponding eigenenergies can be deduced through a simple implicit relation between λ_i and the energy-dependent dielectric constant (see the Appendix). In the case of a model Drude-Lorentz dielectric constant, a general expression for the cSPh eigenenergies is (see the Appendix)

$$\omega_i = \sqrt{\frac{\epsilon_\infty \omega_{\mathrm{LO}}^2(\lambda_i+1) - \omega_{\mathrm{TO}}^2(\lambda_i-1)}{\epsilon_\infty(\lambda_i+1) - (\lambda_i-1)}}. \quad (1)$$

cSPh energies lie between the bulk LO and TO energies, as $-1 < \lambda_i < 1$ [18], and we directly see that the energy of two well-known FK modes for an infinitely thin slab, describing the charge-antisymmetric and charge-symmetric modes [see Fig. 1(a)], are retrieved for $\lambda_i = \pm 1$. In addition, other simple cases can be straightforwardly deduced. $\lambda_i = 0$ corresponds to the abovementioned surface phonon [1] case ($\epsilon = -1$) with eigenenergy $\omega_s = \sqrt{(\epsilon_\infty \omega_{\mathrm{LO}}^2 + \omega_{\mathrm{TO}}^2)/(\epsilon_\infty + 1)}$ in a Drude-Lorentz model, and $\lambda_i = -1/3$ [5] corresponds to the dipolar mode of a sphere ($\epsilon = -2$, $\omega_i = \sqrt{(\epsilon_\infty \omega_{\mathrm{LO}}^2 + 2\omega_{\mathrm{TO}}^2)/(\epsilon_\infty + 2)}$).

To exemplify the interest of this approach, we start with the case of nanorods, which has been widely investigated in surface plasmon physics [19], and especially by EELS [20,21]. The simplicity of the structure makes it easy to understand the intimate link between shape and modes structures, and we adapt it here to the case of a phononic material following arguments for localized SPs found in Ref. [5]. Modes in a nanorod of radius r and length L are similar to the SPh modes of the infinite rod, except that the confinement restricts the available wave vectors to a multiple of $1/2L$. This is exemplified in Fig. 1(c), where the discrete modes dispersion relation, simulated for a large set of nanorod lengths, overlaps the one of an infinite rod. Such modes are the cSPh modes of the nanorod. The cSPh modes disperse between ω_{TO} and ω_s, in analogy with the corresponding dispersion in localized SP in nanorods restricted between 0 and ω_{SP} [5]. Similarly to the corresponding localized SP modes, each mode with eigenvalue λ_i corresponds to an oscillation of the surface eigencharge, as depicted in Fig. 1(d). Despite the fact that simulations have been performed in a retarded approximation (see the Appendix), the nanorod energies follow quite closely the quasistatic dispersion relation (dotted line). This is a strong evidence that in the prototypical case of a nanorod the QS approximation is much more justified for cSPh than for localized plasmons for objects of the same sizes. Indeed, the length [top scale in Fig. 1(c)] of a typical nanorod is much smaller than the equivalent free-space wavelength of the cSPh [right-hand scale in Fig. 1(c)]. Another difference with SPs is the pileup of low-order modes for long nano-antennas close to ω_{TO}, which is obviously absent for localized surface plasmons.

Figure 2(a) presents one EELS spectrum simulated for beam impinging 10 nm away from one tip of a MgO rod 200 nm long and 30 nm in diameter. The simulations performed in the full retarded approximation and using an experimental dielectric constant as an input [22] reveal a series of peaks. As shown in Table I, a direct comparison of their energy values with that of the cSPhs deduced from Eq. (1), which is purely quasistatic and based on the sole knowledge of the λ_i, ω_{TO}, ω_{LO} and ϵ_∞, shows an almost perfect agreement. This validates conceptually our approach, and also allows us to use a simple EELS modal decomposition [see Eq. (A2)] for EELS simulations.

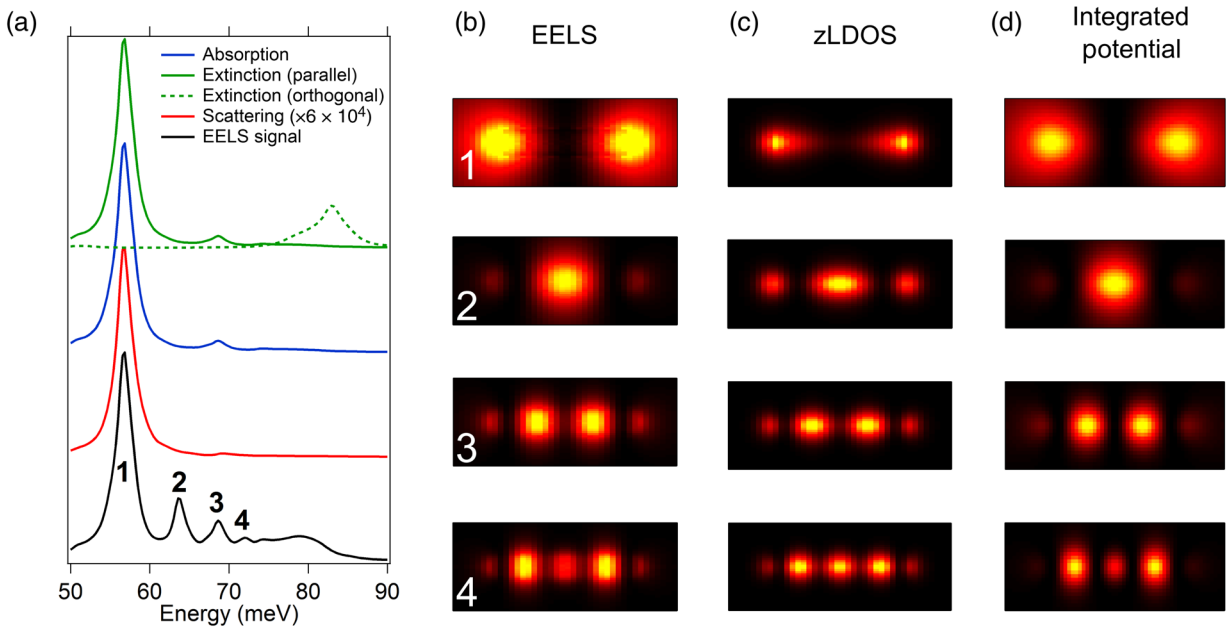

FIG. 2. Optical cross sections, EELS, EMLDOS, and eigenpotentials for the cSPh in a nanorod of MgO. (a) Simulated optical cross sections for an incoming beam propagating perpendicular to the nanorod axis, and EELS spectrum for an electron beam located 10 nm away from one tip of the nanorod. All spectra have been shifted for clarity. Optical cross section scales are the same for extinction and absorption, and multiplied by 6×10^4 for scattering. The polarization of the electrical field is parallel to the nanorod axis, except for the dotted curve. The nanorod is 200 nm in length and 30 nm in diameter. (b) EELS maps for the four first modes of the nanorod. (c) Corresponding zEMLDOS maps taken at $z = 10$ nm from the surface of the rod. (d) Corresponding z-integrated eigenpotentials.

TABLE I. Comparison between energy values for the nanoantenna in Fig. 1(d) calculated with Eq. (1) and as extracted from the simulated spectra in Fig. 2. Inputs for Eq. (1) are $\omega_{TO} = 50.7$ meV, $\omega_{LO} = 91.3$ meV, $\epsilon_\infty = 3.01$ [22]. Simulations have been performed in the full retarded approximation, with the experimental dielectric constant found in Ref. [22].

	Mode 1	Mode 2	Mode 3	Mode 4	Surface
	$\lambda_i = -0.93$	$\lambda_i = -0.80$	$\lambda_i = -0.67$	$\lambda_i = -0.56$	$\lambda_i = 0$
	ω_1 (meV)	ω_2 (meV)	ω_3 (meV)	ω_4 (meV)	ω_s (meV)
From Eq. (1)	56.0	63.4	68.7	72.3	83.1
Simulations [Fig. 2(a)]	56.8	63.6	68.6	72.0	82.9

In Fig. 2(a), we also compare EELS to macroscopic optical quantities such as the absorption, extinction, and scattering cross sections calculated in the retarded approximation. As in the case of EELS, the spectra do not peak at the normal modes energies ω_{LO} and ω_{TO}. Instead, they are dominated by the cSPh modes, in analogy with the well-known case of a slab spectrum dominated by the FK modes [3], or more generally, for an ensemble of nanoparticles [23]. This is particularly justified from the modal decomposition of the cross sections; see Eq. (A3) and Ref. [15]: the optical cross sections are proportional to a spectral function peaking at the dipolar cSPh mode energy. Contrary to the case of EELS, only the dipolar modes are observable (but a very slight contribution from the third-order mode). The spectra obviously show a large dependence on the incoming polarization. For polarizations along the nanorod axis, the dipolar mode of the low-energy branch is excited. For a polarization perpendicular to it, the dipolar modes of the other branches, almost all arising at ω_s [24], are excited; see Fig. 2(a). This points to the fact that EELS is sensitive to both bright (i.e., optically active) and dark (i.e., not optically active) cSPhs, in contrast to optical far-field techniques.

Obtaining truly dark (nonemitting or absorbing) localized SPs is difficult due to the relatively large sizes of plasmonic particles [15] with respect to the corresponding free-space wavelengths. In contrast, for the cSPhs where the QS approximation is justified for much larger particle sizes, almost only dipolar modes are bright. We note that the scattering cross section is several orders of magnitude smaller than the extinction one. This is basically related to the fact that, other things being equal, the ratio between scattering and extinction scales as $1/\omega^3$, where ω is the energy of interest. This makes extinction and absorption cross sections almost identical at the low energy of the phonon regime, making EELS very close to the absorption cross section for dipolar cSPh modes (see also the analytical proof in the Appendix). We note that this contrasts with the case of a silver plasmonic nanorod of the same size (see Fig. 3). In this case, scattering has a major contribution in the extinction cross section.

We can now clarify the type of selection rules when exciting cSPh optically or with electrons. To start with, in the QS approximation, only dipolar modes can be excited by a plane wave, and the electrical polarization of the plane wave must be aligned with the dipole direction. Away from

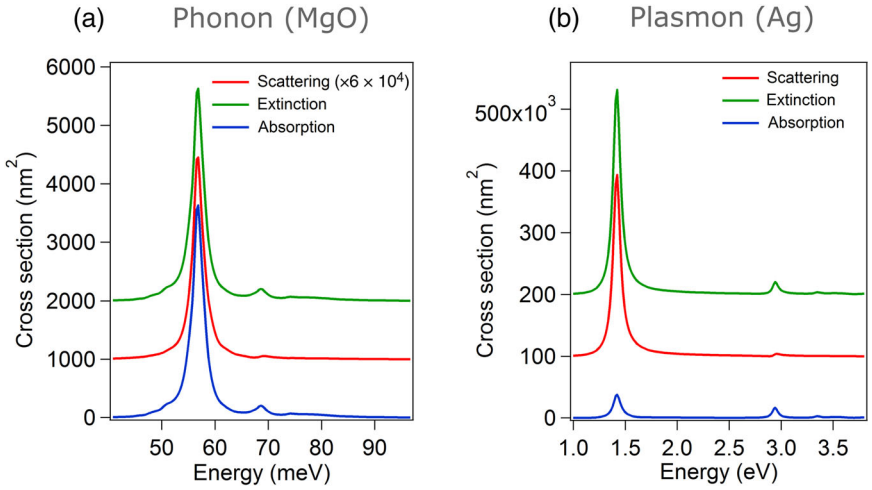

FIG. 3. Optical extinction, absorption, and scattering cross sections for (a) A MgO nanoantenna and (b) a silver nanoantenna. Both antennas have the same size (200 × 30 nm). Note the absolute cross section values.

the QS, similar symmetry arguments arise: even modes [modes 2 and 4 in Fig. 1(b)–1(d)] cannot be excited by a plane wave with the electrical field in the plane containing the axis of the nanoantenna, while odd modes (1 and 3) can be excited. Tilting the beam direction with respect to the antenna axis will break the symmetry and make it possible to also detect even-order modes. More generally, for optical experiments, the selection rules are completely determined by the general symmetry of the surface charge distribution with respect to the plane wave direction and polarization.

The interplay between the symmetries of the incoming electron electrical field and the surface eigencharges is different. As with optics, cSPh modes are also probed by EELS, but contrary to optics, EELS is sensitive to all modes even in the QS approximation. Also, the symmetry of the surface eigencharges impacts rather the spatial distribution of the EELS signal. Indeed, EELS maps [Fig. 2(b)] closely resemble the EMLDOS projected along the electron propagation direction z [zEMLDOS, Fig. 2(c)], with the EMLDOS spatial and spectral distribution being essentially determined by the size, shape, and symmetries of the object of interest. The resemblance between EELS and zEMLDOS is expected by analogy with the localized SP case, where also a general analytical relation between these two quantities can be determined [13]. Much as in the case of localized SPs [14], EELS as well as near-field optical techniques do not map directly the eigencharges [25]. Rather, they map the related zEMLDOS, itself related to the z projection of the electric eigenfield in the QS limit [9,14]. An even more precise description of EELS of cSPh in terms of electromagnetic quantities is given by the almost perfect identity between EELS and the z-integrated eigenpotentials [26]; see Fig. 2(d).

We can sum up the results exemplified on the nanorods but valid for any kind of phononic nanoobject.

First, *surface* EELS and optical IR absorption, extinction, and scattering of nanoparticles probe the same physical excitations, namely cSPh. The symmetry of the cSPh surface eigencharges, which depends on the global shape and symmetry of the subtending particle, determines the coupling strength of the cSPh with the probing electrons or photons. This is in stark contrast with bulk IR absorption or *bulk* EELS [11,27,28], which are probing *normal* modes, which depend on local (atomic) symmetries, i.e., the bulk material properties. This is also a main difference between our work, which relates surface vibrational EELS to the concept of EMLDOS, and recent theoretical works describing the link between bulk EELS to the concept of phononic density of states (pDOS). Again, pDOS is dependent on the atomic structure symmetry while EMLDOS is dependent on the global (shape) symmetry of the nanoparticle. Also, for similar reasons, surface EELS is completely different from Raman spectroscopy, which probes bulk properties of atomic oscillations, although following selection rules different to that of bulk IR absorption. Note that the LCDM can also be used to predict the bulk EELS experiment results through a term proportional to $-\mathrm{Im}[1/\epsilon(\omega)]$, giving essentially a peak at ω_{LO} in the Drude-Lorentz model. The intensity of the related peak may be influenced by the screening at the surface, a phenomenon handled in the LCDM theory and known as the "begrenzung" effect [11]. There are, however, several limits explaining the need to develop dedicated theories for bulk phonons beyond the LCDM [11,27,28], related to the interpretation of angular resolved experiments and possible failure of the local approximation [11,27,28].

Second, EELS maps are close to that obtained with the near-field optical measurement, which is related to the EMLDOS [29], and map quantities close to the cSPh electric eigenfields, and more precisely the eigenpotentials, along the electron direction integrated on the electron beam path [see an analytical proof in Eq. (A2) and Ref. [26]]. The typical spatial extent of the EELS signal is related to that of the EMLDOS, and almost identical to that of the integrated eigenpotentials.

Third, due to the large free-space wavelength of the cSPh compared to typical dimensions of nano-objects, the QS approximation holds essentially true for submicron nanoparticles, and any nanoparticle can be described by a series of eigencharges and related λ_i that depends only on the shape of the nanoparticle.

In addition, this theory works well for understanding cSPhs, but will obviously fail to describe long-wavelength, propagating surface phonons that may arise in the particular case of very large particle or slabs. In the case of slabs or infinite cylinders, however, alternative rigorous retarded theories exist [3]. The differences in the predictions between a quasistatic (such as presented here) and retarded formalism weakly affect lowest-energy, charge-symmetric modes that are usually dominant in slabs and cylinders.

Also, a rigorous modal decomposition of all relevant EELS and optical quantities for arbitrary shaped nanoparticles [see, e.g., Eqs. (A2) and (A3)] is possible, simplifying both the understanding and predictions of surface EELS experiments. Finally, the formalism presented here is not specific to the Drude-Lorentz model [except, of course, Eqs. (1) and (A5)]. Therefore, any situation where a local dielectric constant can be deduced, either theoretically or experimentally, can be handled. For example, *ab initio* models of the IR dielectric constant of a crystal of molecules could be computed, and reinjected in our model for interpreting quantitatively the experiments, just as recently performed by Radtke *et al.* [30] in the case of a planar interface to interpret results on guanine crystals [31]. With all these considerations in mind, we are in position to synthesize observations made in the literature on surface phonons in terms of SPh modes or cSPh modes.

Krivanek *et al.* [17] reported the first observation of vibrational signatures with STEM EELS. Among others, they reported a resonance at 173 meV on a ≈50-nm thick sheet of hexagonal boron nitride (hBN), and a resonance at

TABLE II. Comparison of theoretical and experimental values for $\lambda_i = -1, 1, 0, -1/3$ (charge-symmetric or charge-antisymmetric modes for infinitely thin slabs or cylinders, surface mode, dipolar spherical mode) and experimental values from Refs. [17,33]. In the latter case, two modes (interpreted as charge-symmetric and charge-antisymmetric FK modes) are reported.

		$\lambda_i = -1$	$\lambda_i = 1$	$\lambda_i = 0$	$\lambda_i = -1/3$	
Material	ϵ_∞	ω_{TO} (meV)	ω_{LO} (meV)	ω_s (meV)	ω_d (meV)	Slab Experimental (meV)
SiO_2	2.99 [36]	134 [36]	153 [36]	143.8	140.6	138
hBN (in plane)	4.95 [37]	169 [37]	200 [37]	195		
hBN (out of plane)	4.1 [37]	187 [37]	197 [37]	195		
hBN slab (Ref. [17])						173
hBN slab (experiment, Ref. [33])						187 and 203
hBN slab (theory, Ref. [33])						181 and 197

138 meV in an ≈30-nm thick SiO_2 slab. The resonance energy did not change as a function of the electron beam position whether it was impinging the objects or in vacuum close to them. The 173-meV resonance was attributed to the LO normal mode of hBN, and the other compared to IR results without further assignment. Following the reasoning of this paper, one can rationalize these results; see also Table II. The 173-meV (hBN) modes and 138 meV (SiO_2) are likely to be charge symmetric (lower branch in Fig. 1(a), λ_i close to −1) FK modes. Indeed, with the help of Eq. (1) (see Table II), one can directly deduce that their energies are between the ω_{TO} and ω_s (and very close to $\omega_{TO} =$ 169.5 meV in the case of hBN) but largely different from ω_{LO}; see Table II. For symmetry reasons, the dipole strength of the charge-antisymmetric mode vanishes with the thickness of the slab [32]. It might explain why this mode was not reported in Ref. [17]. On the other hand, as summarized in Table II, Batson and Lagos [33] reported the measurement of two peaks on an hBN flake, the first at 187 meV (below ω_s) and the second at 203 meV (above ω_s). These are likely to be charge-symmetric and charge-antisymmetric modes respectively—as confirmed by preliminary simulations in Ref. [33]—for a slightly thicker slab (as the symmetric mode energy is at higher energy and the symmetric mode is still weaker but now measurable). It is worth noting that in these cases the energy of the modes depends on the geometry and symmetry of the nano-object, and we expect of course the observation of thickness-dependent modes when more experimental works will be available in the literature. Finally, no mode energy spatial variation has been reported on these two sorts of slabs [17,33]. Recently, Schmidt *et al.* [34] showed that the plasmonic modes in thin objects with edges can be decomposed in slab modes and edge modes independently.

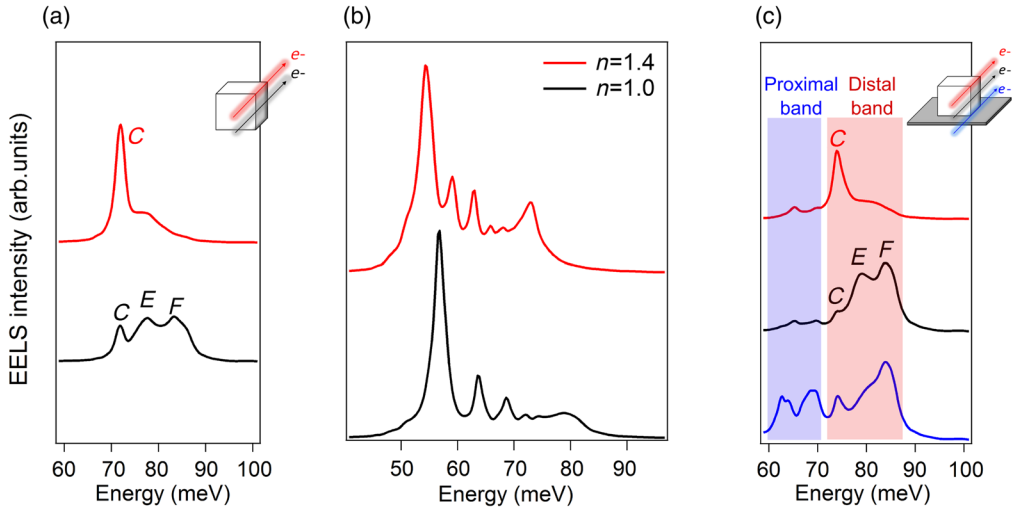

FIG. 4. Dielectric environment effect. (a) Simulated EELS spectra for a cube of MgO (100-nm edge long) in vacuum, exhibiting a corner (C), an edge (E), and a face (F) mode depending on the beam position. (b) Simulated EELS spectra for a nanorod (200 × 30 nm) in vacuum (black) and embedded into a dielectric of refractive index equal to 1.4. The beam is positioned at 10 nm from the tip of the nanorod in both cases. (c) Same simulations as in (a), but for a cube deposited on a substrate of refractive index $n = 2.3$. The former C, E, and F mode split into two bands. The distal band is essentially consisting in a series of C, E, F modes arising at almost the energy of the corresponding vacuum modes, while the proximal band is shifted towards the ω_{TO} energy. Spectra corresponding to a given trajectory are indicated by their colors.

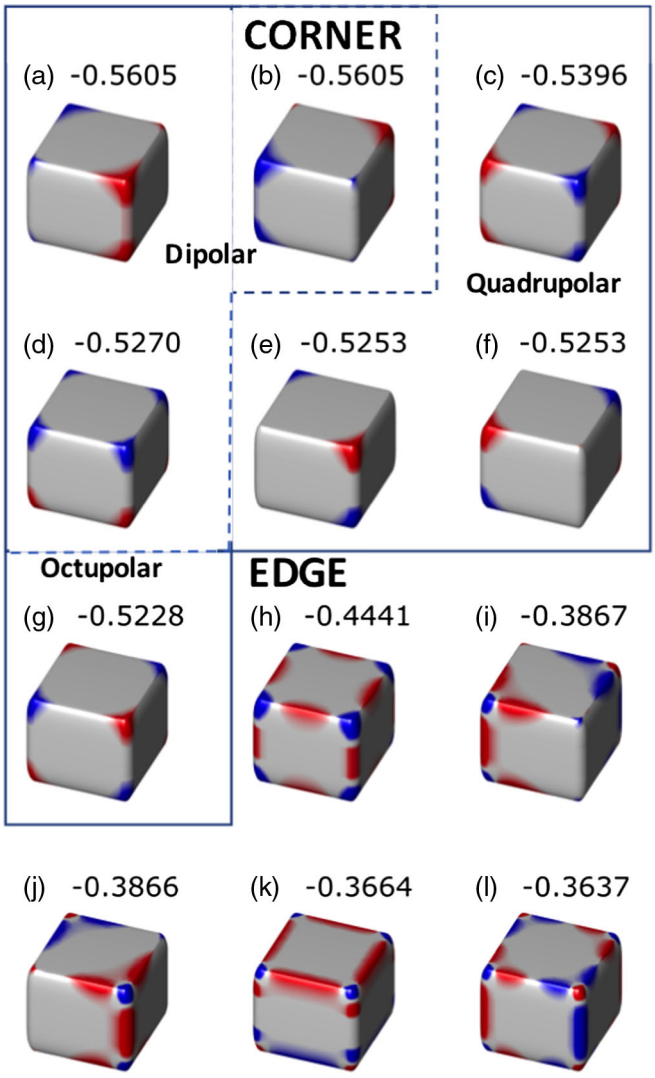

FIG. 5. Modes symmetry for a cube in the quasistatic approximation. Values of λ_i are given on top of the corresponding eigencharge distributions (red is minimum and blue maximum). (a)–(g) Corner modes and (h)–(l) edge modes. Corner modes have been separated with respect to their symmetries.

The slab modes follow the infinite slab dispersion relations, and edges the nanoantennas ones [35]. The modes of lowest-energy branches have the same charge symmetry with respect to the slab or cylinder midplane, so that the slab and edge lowest-energy modes share the same symmetry. Translated to surface phonons in SiO_2 slabs, it means that we should expect two different modes of the same symmetry with respect to the slab midplane; however, both dispersion curves are very close [see, e.g., Fig. 1(a)], and for very thin objects both slab and edge mode energies tend to a unique and same value (ω_{TO}), making it difficult to detect experimentally any spectral or spatial variation except an intensity decrease in vacuum.

In contrast, Lagos *et al.* [11] observed outside of MgO nanocubes an EELS signal with different energies and clear spatial modulations. They identified essentially three modes [see also Fig. 4(a)]: a corner (C) mode at lower energy, an edge (E) mode, and a face (F) mode at higher energies. All the modes could be simulated without taking into account any substrate. Table III sums up the experimental and simulation results of Lagos *et al.*, as well as our simulations and the energies as deduced from Eq. (1). Our simulations are in good agreement with the simulations and experimental results of Lagos *et al.*, not a strong surprise as our simulations and and those of Lagos *et al.* are performed with the same tool (MNPBEM), similar cube parametrization, and the same full retarded approximation. More interestingly, we see in Table III how well Eq. (1) reproduces our simulations and those of Lagos *et al.*, which were pointed out to be in very good agreement with experiments [11]. Our theory gives, however, a stronger insight into the nature of the probed modes. In Ref. [11], modes are denominated through their EELS spatial distribution, with no discussion on their symmetries, which are known to be complex for cube plasmons [38,39]. Indeed, as shown in Fig. 5, the corner mode can be decomposed in dipolar, quadrupolar, and octupolar contributions (see also Table III) that are degenerated in the quasistatic approximation. Because one of its components is dipolar, the corner mode is likely to be bright (i.e., theoretically measurable through an IR extinction experiment) although weakly scattering compared to a plasmonic cube of the same size. Quite interestingly, the edge mode is in fact composed of a large number of cSPhs of close λ_i; see Table III. The symmetry of all these constituting modes makes the edge mode a dark one. Concerning the face mode, the number of polygons required for convergence was too high to deduce a definite value or set of values for λ_i. However, this highest-energy mode has an energy very close to ω_s for MgO, corresponding to $\lambda_i = 0$ (see the Appendix). This is expected from localized SPs analogy, as high momenta modes converge systematically to this value.

We now turn to a point that has not been considered so far but may have important implications for the interpretation of forthcoming experiments. Indeed, the effect of the substrate, known to be essential in plasmon physics, has not been discussed in the context of surface vibrational STEM-EELS experiments. It is well known that localized SP energy and spatial distribution drastically depend on the close presence of other materials, like a substrate or an embedding matrix. In Fig. 4(b), we show the effect of embedding a phononic nanorod into a material of constant dielectric constant different from one. It produces an expected redshift of the excitation, yet still constrained between ω_{TO} and ω_{LO}. The case of a nanoparticle on a substrate is more subtle. In particular, in the case of a nanocube, it is well known from localized SP physics that the modes will split into modes at low energy localized close to the substrate (proximal modes) and at higher energy close to the vacuum (distal modes) [38]. In Ref. [11], only the distal modes were reported, although

TABLE III. Comparison between energy values for the MgO nanocube modes calculated with Eq. (1), from retarded simulations with experimental dielectric constant found in Ref. [22], from retarded simulation in Ref. [11], and from experimental results from Ref. [11]. Inputs for Eq. (1) are $\omega_{TO} = 50.7$ meV, $\omega_{LO} = 91.3$ meV, $\epsilon_\infty = 3.01$ [22]. Energies are given in meV. Note the apparent discrepancy for the face mode values between simulations and experiments, proven in Ref. [11] to be an effect of finite spectral resolution in the experiments.

Mode	Corner						
Symmetry	Dipolar			Quadrupolar			Octupolar
λ_i	−0.56	−0.56	−0.53	−0.53	−0.53	−0.54	−0.52
ω [from Eq. (1)]	72.3	72.3	73.1	73.1	73.1	72.8	73.1
ω (simulations, this paper)				72.0			
ω (simulations, Ref. [11])				72			
ω (experiments, Ref. [11])				69			

Mode	Edge				Face
λ_i	−0.44	−39	⋯	All summed	Not applicable
ω [from Eq. (1)]	75.4	76.5	⋯	Not applicable	Not applicable
ω (simulations, this paper)			77.7		83.3
ω (simulations, Ref. [11])			76		83
ω (experiments, Ref. [11])			72		78

both types of modes are actually predicted (see Fig. 4). We note that the distal mode energies are very close to the mode of a free-space cube, explaining the good agreement between our theory, Lagos *et al.*'s and our simulations without substrate, and experimental results. Observation of the proximal band would however require a spectral resolution even better than is actually available.

Finally, the theory presented here can be extended to understand more complicated situations. This is in analogy with the success of the theory presented for localized SPs [7,13,14,16,18], which has been extended to the 3D mapping of the EMLDOS [40] or of the surface eigencharges [41], the simulation of the cathodoluminescence signals [15,16], the interaction of surface excitations with phase-shaped incoming beams [25], or the coupling between localized SP. Also, this model can be refined by developing a retarded model or a nonlocal approximation extension [42].

This work has received support from the National Agency for Research under the program of future investment TEMPOS-CHROMATEM with the reference ANR-10-EQPX-50.

APPENDIX: MODAL FORM OF SEVERAL OBSERVABLES, ANALOGY BETWEEN SP AND cSPh MODES, TYPICAL MATERIAL VALUES, SIMULATIONS DETAILS

A. Modal form of the cSPh, modal EELS, and application to a Drude-Lorentz model

Following Refs. [7,18], the electromagnetic properties in the quasistatic approximation of an object of dielectric constant $\epsilon(\omega)$ in vacuum can be entirely determined by the set $\{\sigma_i(\vec{s}), \lambda_i\}$, respectively, the surface eigencharge and the eigenvalue for the mode i, i being an integer and $\vec{s}$ the surface position vector. Actual eigenenergies can be determined through the dispersion relation $\lambda_i = (1+\epsilon(\omega_i))/(1-\epsilon(\omega_i))$. From this set, which can be determined numerically [7,12,18], one can deduce all eigenquantities such as the eigenpotential or the electrical eigenfield $\vec{E}_i(\vec{r})$ at all points $\vec{r}$, or any observable such as the EMLDOS $\rho_{\alpha\alpha}(\vec{r},\omega)$ (here, α represents the projection direction),

$$\rho_{\alpha\alpha}(\vec{r},\omega) = \frac{1}{2\pi^2\omega}\sum_i \mathrm{Im}(-g_i(\omega))|E^i_\alpha(\vec{r})|^2, \tag{A1}$$

and the EELS probability (simplified here to the case where the beam is outside of the object of interest) [14],

$$\Gamma(\vec{R}_\perp,\omega) = \frac{1}{\pi\omega^2}\sum_i \mathrm{Im}(-g_i(\omega))|E^i_z(\vec{R_\perp},\omega/v)|^2, \tag{A2}$$

where v is the speed of the electron, z the direction of electron propagation, $\vec{R}_\perp$ the position of the beam in the plane perpendicular to z, and the extinction cross section, which is equal to the absorption cross section in the QS limit, reads [15]

$$C_{\mathrm{ext}}(\omega) \propto \sum_{i,d} A_i \omega \mathrm{Im}(-g_i(\omega)), \tag{A3}$$

where A_i is a mode-dependent prefactor, and the sum runs over the dipolar d cSPh modes only.

$g_i(\omega)$ is a spectral function for mode i depending only on ϵ and λ_i [14] with the imaginary part peaking at the cSPh energy ω_i.

The above formulation clearly points out the fact that the EELS spectra are a superposition of cSPh spectral functions weighted spatially by the modulations of the associated

electrical eigenfields. Also, it shows the close resemblance between EELS and EMLDOS, as well as the spectral similarities between EELS and extinction cross section. In the case where the phonon response can be characterized with LO and TO energies, ω_{LO}, ω_{TO}, a dissipation parameter Γ, and a dielectric constant at large energy ϵ_∞, a Drude-Lorentz form of the dielectric constant reads:

$$\epsilon(\omega) = \epsilon_\infty \left(1 + \frac{\omega_{\mathrm{LO}}^2 - \omega_{\mathrm{TO}}^2}{\omega_{\mathrm{TO}}^2 - \omega^2 + i\omega\Gamma}\right), \tag{A4}$$

then

$$\mathrm{Im}(-g_i(\omega)) = \frac{\Gamma\omega}{(\omega^2-\omega_i^2)^2+\Gamma^2\omega^2}\left[\frac{2(\omega_i^2-\omega_{\mathrm{TO}}^2)^2}{\epsilon_\infty(\omega_{\mathrm{LO}}^2-\omega_{\mathrm{TO}}^2)(1+\lambda_i)}\right]. \tag{A5}$$

The spectral function then takes the simple form of a Lorentzian peaking at the cSPh mode energy ω_i [solution of Eq. (1); this is the energy of the ith cSPh in absence of dissipation], weighted by some energy-independent prefactor.

EMLDOS, EELS, and absorption cross section can be straightforwardly deduced from this expression of the spectral function.

The above deductions can be extended analytically to the case where the object of interest is embedded in a medium. Similar developments (see Supplemental Material of Ref. [16] or Ref. [40]) can be done in the retarded regime assuming a model dielectric function.

B. Analogy between localized SP and cSPh modes

From the point of view of the local continuum dielectric model, there is no functional difference between SPs and surface phonons, SP in slabs and cylinders and FK modes, and localized SP and cSPhs, as long as the details of the dielectric constant are not disclosed. In the case where the SPs are described by a Drude model and the cSPhs by a Drude-Lorentz model, the analogy between SPs and cSPhs can be simply made by replacing ω_{TO} by 0, ω_{LO} by ω_p, and ϵ_∞ by 1. Then, all expressions presented in this paper can be compared to that for SPs, especially those found in Ref. [14]. For example, one retrieves the familiar values of $\omega_p/\sqrt{2}$ and $\omega_p/\sqrt{3}$ for the surface and dipolar surface plasmons.

C. Normal mode, surface phonon, and dipolar surface phonons for some materials

For SiO_2 and MgO, the energy of simple FK and cSPh modes can be straightforwardly deduced from Eq. (1) and the values given in Table II. Limit analytical cases for the energy of the surface phonon (ω_s), the charge-symmetric and charge-antisymmetric FK modes for an infinitely thin slab (converging to ω_{TO} and ω_{LO}), and the dipolar mode for a sphere (ω_d) are given in the main text. Main values calculated with Eq. (1) are given in Table II.

The case of hBN is a bit more involved, as hBN is a uniaxial anisotropic material. Nevertheless, the FK theory can be extended to anisotropic materials for slabs [4]. The charge-symmetric mode converges to the in-plane TO mode energy $\omega_{\mathrm{TO}_\perp}$ and the charge-antisymmetric mode to the out-of-plane LO mode energy $\omega_{\mathrm{LO}_\parallel}$. The terminology $\perp, \parallel$ is related to the anisotropy axis. Likewise, the surface phonon energy will be a combination of in-plane and out-of-plane phonon energy given by the condition $\sqrt{\epsilon_\perp \epsilon_\parallel} = -1$, with $\epsilon_\perp$ and $\epsilon_\parallel$ the in- and out-of-plane dielectric constant [43]. We note that a HREELS study [44] reported a value for the LO mode of a single hBN sheet around 173 meV, similar to the value reported by Ref. [17]. Given the similarities pointed out in the paper between HREELS and STEM EELS and the symmetry arguments, the reported LO mode is most likely to rather be a charge-symmetric FK mode.

D. Simulations

Dispersion relations in Figs. 1(a) and 1(b) have been calculated using formulas from Ref. [45] and using a Drude model adapted to silver and a Drude-Lorentz adapted to MgO. All the other simulations have been carried out using the MNPBEM toolbox [12] using experimental values for the dielectric function of the MgO [22]. Figure 1(d) has been calculated using the quasistatic eigensolver while Figs 1(c), 2, 4, and 5 employ a retarded formulation of the Maxwell equations. Rods have been simulated using approximately 1000 polygons, cubes in vacuum with 5000 polygons, and cubes on substrate with 5000 polygons as well. We simulated a 100-nm long cube with approximately 6000 polygons and calculated the corresponding eigencharges and geometrical eigenvalues λ_i using the PLASMONMODE solver. The radii of curvature of the cube corners in the xy plane are fixed at 3 nm. The rounding in the yz (xz) direction is not precisely controlled within the MNPBEM toolbox [12] (when using the tripolygon and edgeprofile functions). However, we estimate the radius of curvature in these planes to be much shorter than 3 nm. Because of the slight asymmetry of the mesh, the three dipoles (quadrupole and edge dipolar) are slightly non-degenerated; see λ_i values in Fig. 5.

[1] H. Ibach, *Optical Surface Phonons in Zinc Oxide Detected by Slow-Electron Spectroscopy*, Phys. Rev. Lett. **24**, 1416 (1970).

[2] Ph. Lambin, L. Henrard, P. Thiry, C. Silien, and J. P. Vigneron, *The Dielectric Theory of HREELS, A Short*

Survey, J. Electron Spectrosc. Relat. Phenom. **129**, 281 (2003).
[3] R. Fuchs and K. L. Kliewer, *Optical Modes of Vibration in an Ionic Crystal Slab*, Phys. Rev. **140**, A2076 (1965).
[4] K. L. Kliewer and R. Fuchs, *Theory of Dynamical Properties of Dielectric Surfaces*, Adv. Chem. Phys. **27**, 355 (1974).
[5] M. Kociak and O. Stéphan, *Mapping Plasmons at the Nanometer Scale in an Electron Microscope*, Chem. Soc. Rev. **43**, 3865 (2014).
[6] R. Ruppin, *Electromagnetic Scattering from Finite Dielectric Cylinders*, J. Phys. D **23**, 757 (1990).
[7] F. J. García de Abajo and J. Aizpurua, *Numerical Simulation of Electron Energy Loss Near Inhomogeneous Dielectrics*, Phys. Rev. B **56**, 15873 (1997).
[8] F. J. García de Abajo and A. Howie, *Retarded Field Calculation of Electron Energy Loss in Inhomogeneous Dielectrics*, Phys. Rev. B **65**, 115418 (2002).
[9] U. Hohenester, H. Ditlbacher, and J. R. Krenn, *Electron-Energy-Loss Spectra of Plasmonic Nanoparticles*, Phys. Rev. Lett. **103**, 106801 (2009).
[10] N. Geuquet and L. Henrard, *EELS and Optical Response of a Noble Metal Nanoparticle in the Frame of a Discrete Dipole Approximation*, Ultramicroscopy **110**, 1075 (2010).
[11] M. J. Lagos, A. Trügler, U. Hohenester, and P. E. Batson, *Mapping Vibrational Surface and Bulk Modes in a Single Nanocube*, Nature (London) **543**, 529 (2017).
[12] U. Hohenester, *Simulating Electron Energy Loss Spectroscopy with the MNPBEM Toolbox*, Comput. Phys. Commun. **185**, 1177 (2014).
[13] F. J. García de Abajo and M. Kociak, *Probing the Photonic local density of states with electron energy loss spectroscopy*, Phys. Rev. Lett. **100**, 106804 (2008).
[14] G. Boudarham and M. Kociak, *Modal decompositions of the local electromagnetic Density of States and Spatially Resolved Electron Energy Loss Probability in Terms of Geometric Modes*, Phys. Rev. B **85**, 245447 (2012).
[15] A. Losquin, L. F. Zagonel, V. Myroshnychenko, B. Rodríguez-González, M. Tencé, L. Scarabelli, J. Förstner, L. Liz-Marzán, F. J. García de Abajo, O. Stéphan, and M. Kociak, *Unveiling Nanometer Scale Extinction and Scattering Phenomena through Combined Electron Energy Loss Spectroscopy and Cathodoluminescence Measurements*, Nano Lett. **15**, 1229 (2015).
[16] A. Losquin and M. Kociak, *Link between Cathodoluminescence and Electron Energy Loss Spectroscopy and the Radiative and Full Electromagnetic Local Density of States*, ACS Photonics **2**, 1619 (2015).
[17] O. L. Krivanek, T. C. Lovejoy, N. Dellby, T. Aoki, R. W. Carpenter, P. Rez, E. Soignard, J. Zhu, P. E. Batson, M. J. Lagos, R. F. Egerton, and P. A. Crozier, *Vibrational Spectroscopy in the Electron Microscope*, Nature (London) **514**, 209 (2014).
[18] F. Ouyang and M. Isaacson, *Surface Plasmon Excitation of Objects with Arbitrary Shape and Dielectric Constant*, Philos. Mag. B **60**, 481 (1989).
[19] L. Novotny and N. van Hulst, *Antennas for Light*, Nat. Photonics **5**, 83 (2011).
[20] D. Rossouw, M. Couillard, J. Vickery, E. Kumacheva, and G. A. Botton, *Multipolar Plasmonic Resonances in Silver Nanowire Antennas Imaged with a Subnanometer Electron Probe*, Nano Lett. **11**, 1499 (2011).
[21] I. Alber, W. Sigle, S. Muller, R. Neumann, O. Picht, M. Rauber, P. A. van Aken, and M. E. Toimil-Molares, *Visualization of Multipolar Longitudinal and Transversal Surface Plasmon Modes in Nanowire Dimers*, ACS Nano **5**, 9845 (2011).
[22] A. M. Hofmeister, E. Keppel, and A. K. Speck, *Absorption and Reflection Infrared Spectra of MgO and Other Diatomic Compounds*, Mon. Not. R. Astron. Soc. **345**, 16 (2003).
[23] R. Fuchs, *Theory of Optical-Properties of Ionic-Crystal Cubes*, Phys. Rev. B **11**, 1732 (1975).
[24] R. Gomez-Medina, N. Yamamoto, M. Nakano, and F. J. G. Abajo, *Mapping Plasmons in Nanoantennas via Cathodoluminescence*, New J. Phys. **10**, 105009 (2008).
[25] G. Guzzinati, H. Béché, A. Lourenço-Martins, J. Martin, M. Kociak, and J. Verbeeck, *Probing the Symmetry of the Potential of Localised Surface Plasmon Resonances with Phase-Shaped Electron Beams*, Nat. Commun. **8**, 14999 (2017).
[26] A. Hörl, A. Trügler, and U. Hohenester, *Tomography of Particle Plasmon Fields from Electron Energy Loss Spectroscopy*, Phys. Rev. Lett. **111**, 076801 (2013).
[27] C. Dwyer, T. Aoki, P. Rez, S. L. Y. Chang, T. C. Lovejoy, and O. L. Krivanek, *Electron-Beam Mapping of Vibrational Modes with Nanometer Spatial Resolution*, Phys. Rev. Lett. **117**, 256101 (2016).
[28] B. D. Forbes and L. J. Allen, *Modeling Energy-Loss Spectra due to Phonon Excitation*, Phys. Rev. B **94**, 014110 (2016).
[29] R. Hillenbrand, T. Taubner, and F. Keilmann, *Phonon-Enhanced Light-Matter Interaction at the Nanometre Scale*, Nature (London) **418**, 159 (2002).
[30] G. Radtke, D. Taverna, M. Lazzeri, and E. Balan, *First-Principles Vibrational Electron Energy Loss Spectroscopy of β-Guanine*, Phys. Rev. Lett. **119**, 027402 (2017).
[31] P. Rez, T. Aoki, K. March, D. Gur, O. L. Krivanek, N. Dellby, T. C. Lovejoy, S. G. Wolf, and H. Cohen, *Damage-Free Vibrational Spectroscopy of Biological Materials in the Electron Microscope*, Nat. Commun. **7**, 10945 (2016).
[32] O. Stéphan, D. Taverna, M. Kociak, K. Suenaga, L. Henrard, and C. Colliex, *Dielectric Response of Isolated Carbon Nanotubes Investigated by Spatially Resolved Electron Energy-Loss Spectroscopy: From Multiwalled to Single-Walled Nanotubes*, Phys. Rev. B **66**, 155422 (2002).
[33] P. E. Batson and M. J. Lagos, *Characterization of Misfit Dislocations in Si Quantum Well Structures Enabled by STEM Based Aberration Correction*, Ultramicroscopy **180**, 34 (2017).
[34] F. P. Schmidt, H. Ditlbacher, U. Hohenester, A. Hohenau, F. Hofer, and J. R. Krenn, *Universal Dispersion of Surface Plasmons in Flat Nanostructures*, Nat. Commun. **5**, 3604 (2014).
[35] A. Campos, A. Arbouet, J. Martin, D. Gérard, J. Proust, J. Plain, and M. Kociak, *Plasmonic Breathing and Edge Modes in Aluminum Nanotriangles*, ACS Photonics **4**, 1257 (2017).
[36] M. Fujii, M. Wada, S. Hayashi, and K. Yamamoto, *Infrared Absorption in* SiO_2*-Ge Composite Films: Influences of Ge*

Microcrystals on the Longitudinal-Optical Phonons in SiO_2, Phys. Rev. B **46**, 15930 (1992).

[37] R. Geick, C. H. Perry, and G. Rupprecht, *Normal Modes in Hexagonal Boron Nitride*, Phys. Rev. **146**, 543 (1966).

[38] S. Zhang, K. Bao, N. J. Halas, H. Xu, and P. Norlander, *Substrate-Induced Fano Resonances of a Plasmonic Nanocube: A Route to Increased-Sensitivity Localized Surface Plasmon Resonance Sensors Revealed*, Nano Lett. **11**, 1657 (2011).

[39] S. Mazzucco, N. Geuquet, J. Ye, O. Stéphan, W. Van Roy, P. Van Dorpe, L. Henrard, and M. Kociak, *Ultralocal Modification of Surface Plasmons Properties in Silver Nanocubes*, Nano Lett. **12**, 1288 (2012).

[40] A. Hörl, A. Trügler, and U. Hohenester, *Full Three-Dimensonal Reconstruction of the Dyadic Green Tensor from Electron Energy Loss Spectroscopy of Plasmonic Nanoparticles*, ACS Photonics **2**, 1429 (2015).

[41] S. M. Collins, E. Ringe, M. Duchamp, Z. Saghi, R. E. Dunin-Borkowski, and P. A. Midgley, *Eigenmode Tomography of Surface Charge Oscillations of Plasmonic Nanoparticles by Electron Energy Loss Spectroscopy*, ACS Photonics **2**, 1628 (2015).

[42] F. J. Garcia de Abajo, *Optical Excitations in Electron Microscopy*, Rev. Mod. Phys. **82**, 209 (2010).

[43] M. Kociak, O. Stéphan, L. Henrard, V. Charbois, A. Rothschild, R. Tenne, and C. Colliex, *Experimental Evidence of Surface-Plasmon Coupling in Anisotropic Hollow Nanoparticles*, Phys. Rev. Lett. **87**, 075501 (2001).

[44] C. Oshima and A. Nagashima, *Ultra-Thin Epitaxial Films of Graphite and Hexagonal Boron Nitride on Solid Surfaces*, J. Phys. Condens. Matter **9**, 1 (1997).

[45] A. Rivacoba, N. Zabala, and J. Aizpurua, *Image Potential in Scanning Transmission Electron Microscopy*, Prog. Surf. Sci. **65**, 1 (2000).